Title

Aligned Al:ZnO nanorods on Si with different barrier layers for optoelectronic applications

Journal

Chemical Physics Letters, 534

ISSN

00092614

Authors

Holloway, Terence
Mundle, Rajeh
Dondapati, Hareesh
et al.

Publication Date

2012-05-01

DOI

10.1016/j.cplett.2012.03.028

Peer reviewed

Chemical Physics Letters 534 (2012) 48–53

Contents lists available at SciVerse ScienceDirect

Chemical Physics Letters

journal homepage: www.elsevier.com/locate/cplett

Aligned Al:ZnO nanorods on Si with different barrier layers for optoelectronic applications

Terence Holloway, Rajeh Mundle, Hareesh Dondapati, M. Bahoura, A.K. Pradhan *

Center for Materials Research, Norfolk State University, 700 Park Ave., Norfolk, VA 23504, USA

ARTICLE INFO

Article history:
Received 3 January 2012
In final form 6 March 2012
Available online 14 March 2012

ABSTRACT

We report almost perfectly vertically aligned ZnO nanorod arrays synthesized by the hydrothermal route at considerably lower temperature on a sputtered Al:ZnO seed layer using different growth strategies. The nanorod arrays demonstrate remarkable alignment along the *c*-axis over a large area. Several barrier layers, such as ZnO, Al_2O_3, $BaTiO_3$ and SiO_2, were introduced to form the p-i-n junction to reduce the leakage current. The photocurrent is significantly reduced in nanorod arrays on AZO/SiO_2/*p*-Si heterojunction due to multiple scattering phenomena from ZnO hexagonal facets associated with the nanorod arrays. This research may open up venues for various optical and opto-electronic applications where highly aligned nanostructures are desired.

1. Introduction

Nanorods are becoming important materials for photovoltaic, gas sensors, biosensors and multitude of other applications. Nanorods have been used to increase *pn*-junction area in dye-sensitized solar cells and in polymer semiconductor hybrid solar cells. Electrodes consisting of nanorods in double layer capacitors increased the energy storage capacity and could lead to faster charging times. Vertically aligned nanorod arrays provide a simple matrix to study the average effect of assembled nanorods [1–4]. One-dimensional (1-D) semiconductor nanomaterials have been attracting increasing attention due to their outstanding properties, which are different from bulk materials. Particularly, well-aligned ZnO nanorod arrays show great potential for solar cell applications [5,6]. Nanorods have been used to increase *pn*-junction area in dye-sensitized solar cells [7] and in polymer semiconductor hybrid solar cells [8]. High mobility nanorods are pathways for exciton diffusion into *pn*-junctions in solar cells [9]. The charge transport as well as tailoring of band gap by either doping or quantum confinement due to size effects are considered to be very import issues for the application of semiconductor nanostructures, especially for solar cell applications. In order to investigate the doping effect, change occurred only by doping must be identified. When dopants are introduced during the forming process of nanostructures, they affect the optical properties of ZnO nanostructures. Furthermore, template-free (for example, not using porous alumina template) well aligned growth of nanostructure on the microstructural and optical characteristics of the solution-grown Al-doped ZnO nanorod arrays have significant impact for optical, electronic and opto-electronic applications. ZnO is a direct n-type semiconductor with a Wurtzite hexagonal structure, having a wide bandgap (3.33 eV at room temperature) and a large exciton binding energy (60 meV). Highly oriented vertical nanorod arrays are highly desired for their future application in various fields like nanoelectronic or photoelectronic materials where one-dimensional directionality is needed (lasing, photonic effects, etc.). Also, light scattering properties are under intense focus for application in the field of solar cells in order to enhance the absorption of light in thin absorber layers.

In this Letter, we report almost perfectly vertically aligned ZnO nanorod arrays synthesized by the hydrothermal route at 95 °C on a sputtered Al:ZnO seed layer. The nanorod arrays demonstrate remarkable alignment along the *c*-axis over a large area. The electrical properties of the seed layers as well as the nanorod arrays were investigated. The optoelectronic properties, such as photovoltaic of nanorod arrays on Al:ZnO/*p*-Si seed layer with various barrier layers have been illustrated.

2. Experimental details

Al:ZnO (AZO) seed layer films were deposited to Boron doped *p*-Si and glass substrates by rf sputtering technique using an Ar pressure of 2.2 mTorr, rf power of 150 W, and the deposition temperature at 350 °C for the deposition time of 20–30 min. An AZO (2 wt.% Al_2O_3 in ZnO) ceramic target was used to deposit the AZO seed layer film. The Si substrate was cleaned using a mixture of HF:H_2O (1:10) in order to remove SiO_2 and achieve H-terminated surface.

AZO nanorod arrays were grown by the hydrothermal method. The AZO seed laree coated samples were placed in an aqueous solution (50 ml) of different molarity concentration of 0.1, 0.05 M zinc nitrate ($Zn(NO_3)_2$), 0.1, 0.05 M hexamethylenetetramine

* Corresponding author.
E-mail address: apradhan@nsu.edu (A.K. Pradhan).

0009-2614/$ - see front matter © 2012 Elsevier B.V. All rights reserved.
http://dx.doi.org/10.1016/j.cplett.2012.03.028

(HMT), and different wt.% (1%, 5%, 10%) of Al doping. For Al doping two different chemicals, $AlCl_3$ and $Al(NO_3)_2$, were used to explore the effect of each chemical on the growth parameters of the nanorod arrays. All precursors were dissolved in deionized water. A glass bottle with the cap screwed on tightly was used and heated in a silicon oil bath at a 95 °C, for 2–4 h. At the end of the growth period, the samples were cooled to room temperature and removed from the solution. Then the samples were immediately rinsed with deionized water to remove any residual salt from the surface. Finally, the samples were blown with nitrogen and dried

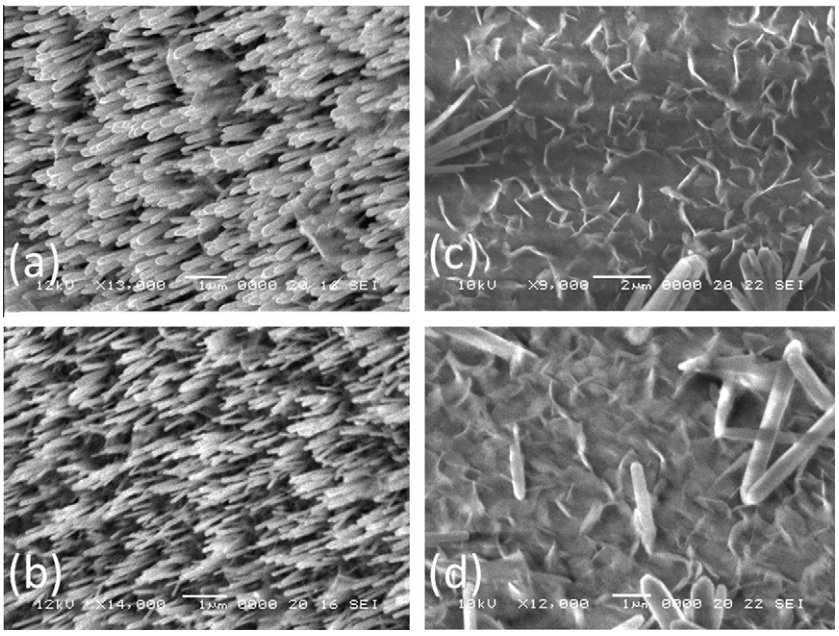

Figure 1. (a) 1 wt.%-0.05 M, (b) 5 wt.%-0.05 M, (c) 10 wt.%-0.05 M, and (d) 10 wt.%-0.05 M, enlarge scale. $AlCl_3$ was used for Al doping.

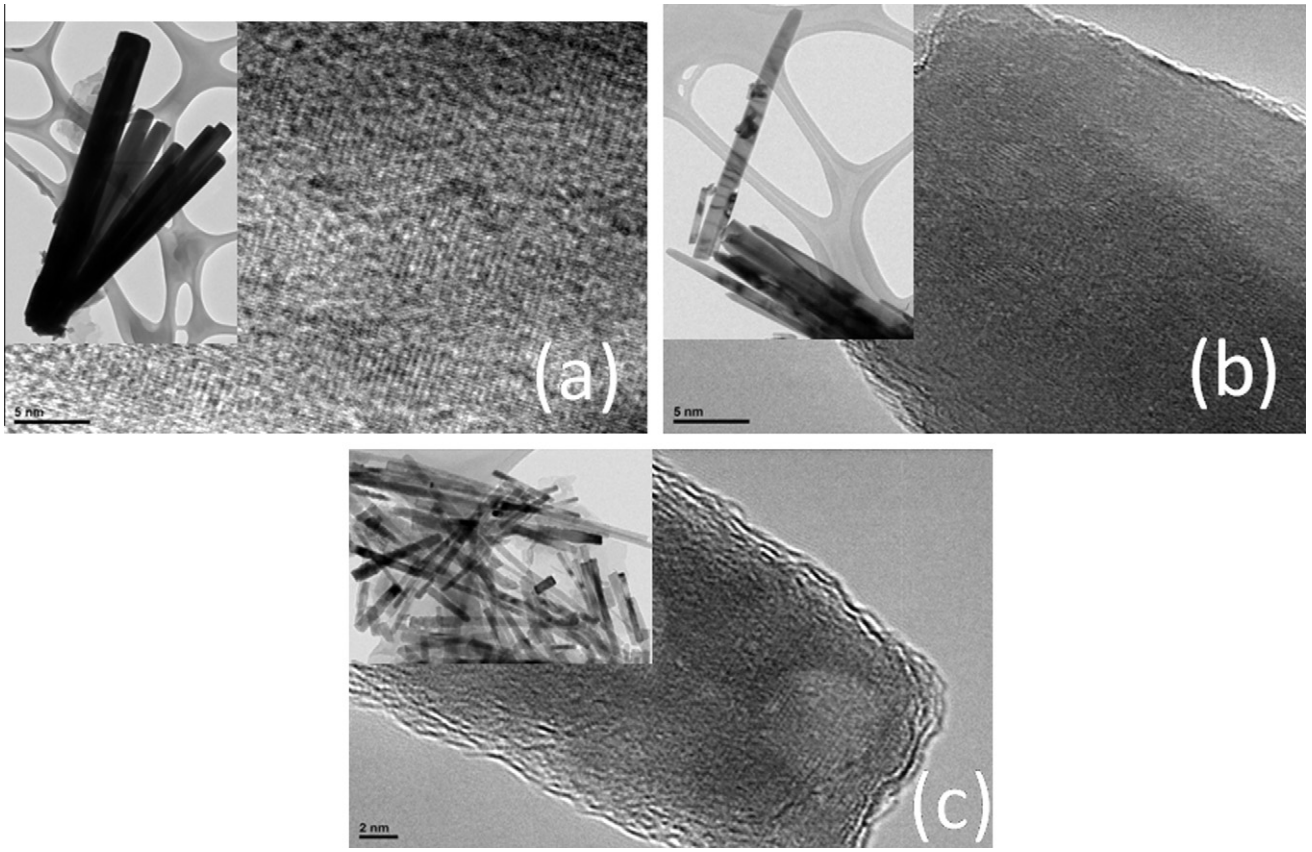

Figure 2. (a) 1 wt.%-0.05 M, (b) 5 wt.%-0.05 M, and (c) 10 wt.%-0.05 M. $AlCl_3$ was used for Al doping.

in air in an oven at 100 °C for 10–15 min. It is noted that we report here only for one concentration, i.e., 5 wt.% of Al doping by nitrate precursors.

Thickness measurement of the seed layer was performed using Dektak profilometer, and found to be about 150 nm. The XRD measurements were performed on a Rigaku powder X-ray diffractometer with CuKα incident radiation ($\lambda = 1.5405$ Å) to examine the crystallographic structure. X-ray diffraction studies show intense (002) peak, indicating Wurtzite structure and most of the nanorods grow with their *c*-axis normal to the surface, indicating that the nanorod arrays aligned vertically to the surface of the seed layer. In further examination of the XRD curves, a gradual increase in the (100), (002), and (101) peak intensity was seen with annealing temperature, indicative of improved crystallinity. Some of the XRD patterns, for example, for AZO nanorods grown with different Al wt.% (1%, 5%, 10%) using 0.05 M $AlCl_3$ as well as using 0.05 M $Al(NO_3)_2$ (Supplementary information, Fig. S1a and b, respectively) indicate the random orientation of nanorods as well as very good oriented nanorods with Wurtzite structure and hexagonal phase depending on the growth precursors.

Transmission electron microscope (TEM) to determine the crystal structure and morphology, field emission-scanning electron microscope (FE-SEM), Hitachi 4700 scanning electron microscope, as well as scanning electron microscope (SEM), JEOL JSM-5900LV, were used to examine the surface morphology and orientation of the nanorods arrays. The elemental composition analysis of the seed layer and nanorods (Supplementary information, Fig. S1c and d, respectively) was performed by energy dispersive spectroscopy (EDS). This indicates the AZO seed layer and nanorod arrays composition. Zinc, oxygen and aluminum peaks have been observed on the spectrum. The Al composition in nanorod is observed to be less.

The optical absorption was measured by UV–VIS–IR spectrophotometer (Perkin Elmer Lambda 950 UV–VIS–IR). Temperature dependence of the electrical resistivity was measured using a four-probe technique. The photocurrent was measured from the current–voltage characteristics using a solar simulator.

3. Results and discussion

Figure 1 presents the SEM images of (a) Al-1 wt.%-0.05 M, (b) Al-5 wt.%-0.05 M, (c) Al-10 wt.%-0.05 M, and (d) Al-10 wt.%-0.05 M in an enlarge scale. $AlCl_3$ was used for Al doping. It is interesting to note that the nanorod arrays grow vertically for both Al concentration of 1 and 5 wt.% at a fixed molarity 0.05 M concentration of $Zn(NO_3)_2$. However, for the same molar concentration of 0.05 M, nanorod arrays did not grow.

It is interesting to note that the nanorods grow for molarity of 0.05 M while $AlCl_3$ was used for Al doping from 1 to 10 wt.% as illustrated in the TEM images of inset of Figure 2. The superior crystalline quality of the nanorods is also demonstrated in the TEM images as shown in Figure 2 for all doping levels. The HR-TEM images clearly show that the nanorods are almost free from impurities. The electron dispersive X-ray spectroscopy (EDX) studies show that Al concentration increases from 0.9 wt.% to about

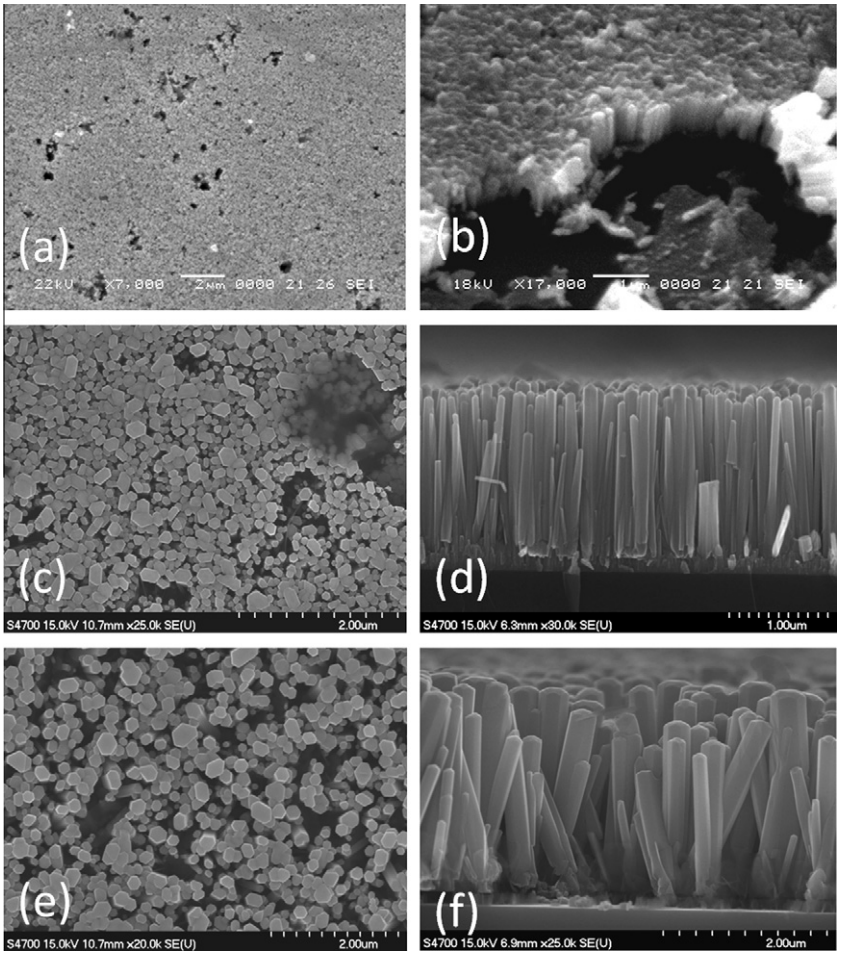

Figure 3. (a and b) 1 wt.%-0.1 M, (c and d) 5 wt.%-0.1 M, and (e and f) 10 wt.%-0.05 M. $AlCl_3$ was used for Al doping.

3 wt.% in nanorods as Al concentration increases in the solution from 1 to 5 wt.%. However, Al concentration fluctuates for 10 wt.% of Al in the solution.

Figure 3 shows the top and side view of SEM images of (a and b) 1 wt.%-0.1 M, (c and d) 5 wt.%-0.1 M, and (e and f) 10 wt.%-0.05 M, where $AlCl_3$ was used for Al doping. Well-defined hexagonal nanorod tops are visible. Although the nanorods are aligned in all concentration of Al, it is well organized and upright for 5 wt.% of Al. However, well-aligned nanorod arrays were grown when $Al(NO)_3$ was used for Al doping as shown in Figure 4. For Al doping of 5 wt.%, a remarkable alignment of nanorod arrays was seen. The density of nanorod arrays varies from 4×10^9, 3.2×10^9, and 2.7×10^9 with a typical nanorod length of 1–1.5 μm as Al doping is increased from 1, 5 and 10 wt.%.

Figure 5 shows the temperature-dependent resistivity curves in order to compare the resistivity of AZO on glass and *p*-Si substrates grown at 350 °C. The resistivity measurements were performed using the four probe techniques using Au contact pads. The temperature-dependent resistivity curves show the typical behavior of a degenerate semiconductor. When n-type semiconductors are heavily doped with Al ion donors, the semiconductor shows a metal-like property in the resistivity. At high doping levels, the donor atoms become so close to each other that it forms a degenerate semiconductor in which the Fermi level lies within the conduction band, similar to the case of metal [10]. The important characteristic in the graph is the observation of the metal-like and metal–semiconductor transition (MST) behavior. The MST was noticed in the vicinity of 125–130 K for the current films. However, the resistivity

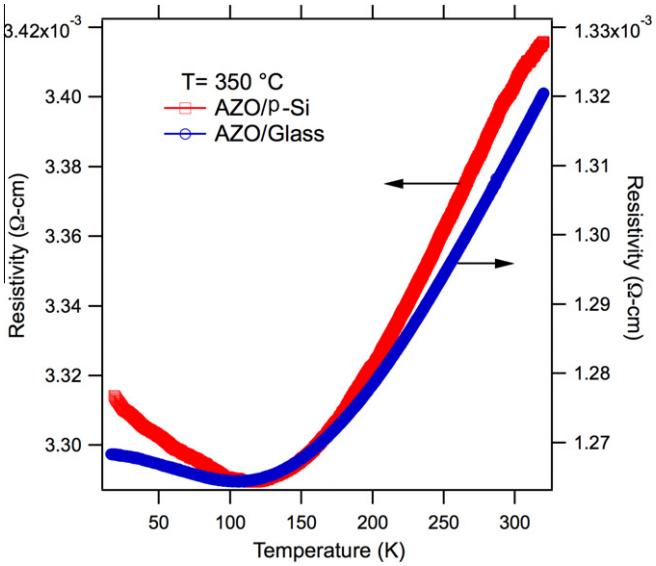

Figure 5. Resistivity vs. temperature of AZO thin-film deposited by RF magnetron sputtering on *p*-Si and glass.

continues decreasing down to $T = 100$ K, showing a characteristic residual resistivity behavior at low temperature which is generally found in an impure metal. The MST temperature describes the semiconductor material as it transitions from an insulating phase

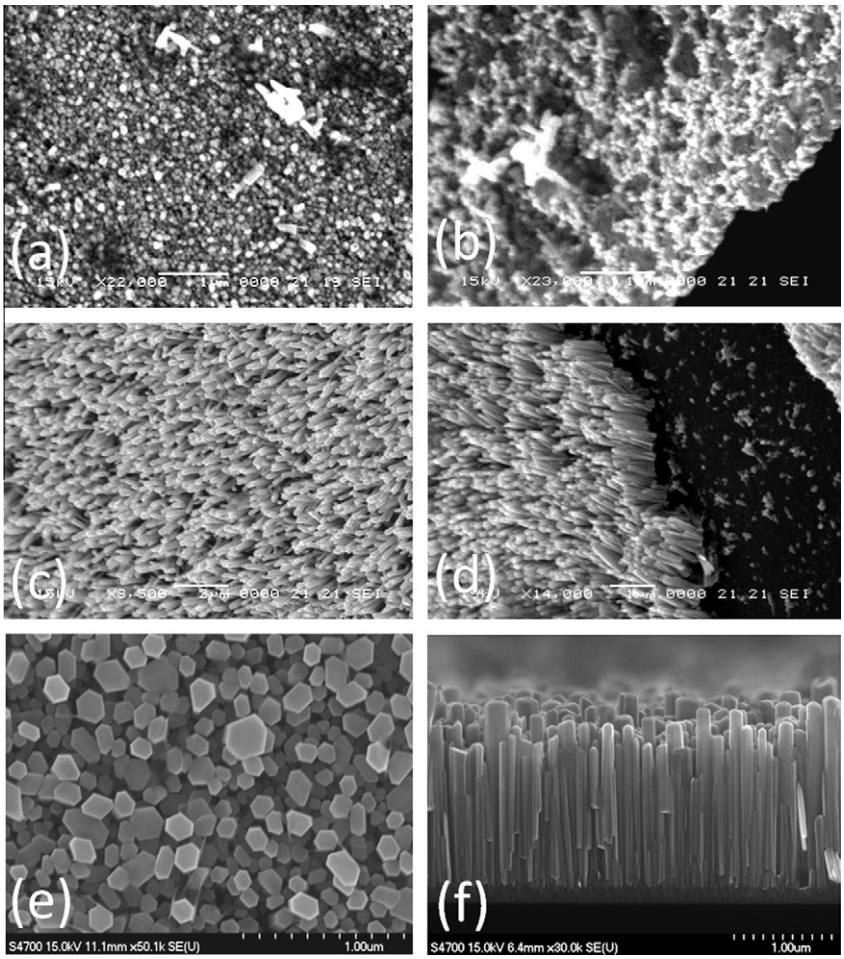

Figure 4. (a and b) 1 wt.%-0.1 M, (c and d) 5 wt.%-0.1 M, and (e and f) 10 wt.%-0.05 M. $Al(NO)_3$ was used for Al doping.

to a metallic phase. To the left of the transition temperature is the insulating phase. As the temperature increases, the resistance decreases. To the right of the transition temperature is the metallic phase. As the temperature increases, the resistance increases. The observed metal-like and metal–semiconductor transitions are explained by taking into account the Mott phase transition in the framework of localization effects [11] as well as the competition between the thermally activated carriers and scattering effects of free carriers in a degenerate semiconductor. The lower resistivity of the AZO/glass films grown can be explained due to the Burstein–Moss effect that an increase of the Fermi level in the conduction band of a degenerate semiconductor leads to an energy band widening. The films showed a positive temperature coefficient of resistance (TCR) above MST and a negative TCR below it. The positive TCR metal-type conductivity behavior can be explained by the formation of a degenerate band appearing in heavily doped semiconductors as suggested by Mott, and found in other doped ZnO semiconductors such as Ga:ZnO_4, Al:ZnO, Nb:TiO_2, and As- and Er-doped ZnO [12–17]. Alternatively, the MST transition can also be explained taking into account the percolation phenomenon, especially in the presence of metallic and semiconductor like networks, which facilitate competition between two types of conduction. Recently, the tunneling conductance in semiconducting nanotubes was modeled considering the possibility of inter-shell hopping [18]. However, this is beyond the scope of the present Letter.

Figure 6 shows the dark current density vs. voltage characteristics of the seed layer with various intermediate layers, such as SiO_2, $BaTiO_3$ (BTO), ZnO, Al_2O_3. This shows the different electrical behavior of the intermediate layers on the AZO/*p*-Si structure. Figure 6 shows that the overall leakage dark current densities for all the samples are smaller than 15 mA/cm^2. One of the samples, AZO/SiO_2/*p*-Si, was annealed in air at 550 °C for 1 h at a rate of 25 °C per min. AZO/ZnO/*p*-Si has linear Ohmic behavior in the reverse and forward bias region. It has a small dark leakage current density of about 3 mA/cm^2. While other samples with SiO_2, BTO and Al_2O_3 with barrier layers have very small dark leakage current less than 2 mA/cm^2.

Figure 7 shows the current density vs. voltage characteristics of AZO/SiO_2/*p*-Si. The dark leakage current density is about 0.4 mA/cm^2 in the reverse bias region. The dark leakage current was reduced while its photocurrent induced under illumination was noticeably larger. It is known that under reverse bias, the current is affected by light. Under light, the photogenerated current density is about 0.7 mA/cm^2 in the reverse bias region. The graph shows a typical rectifying behavior for both cases. In the presence of light a photovoltaic behavior is observed. The short circuit current J_{sc} was $\sim 6.93 \times 10^{-5}$ A/cm^2. The open circuit voltage V_{oc} was about 1.97×10^{-1} V.

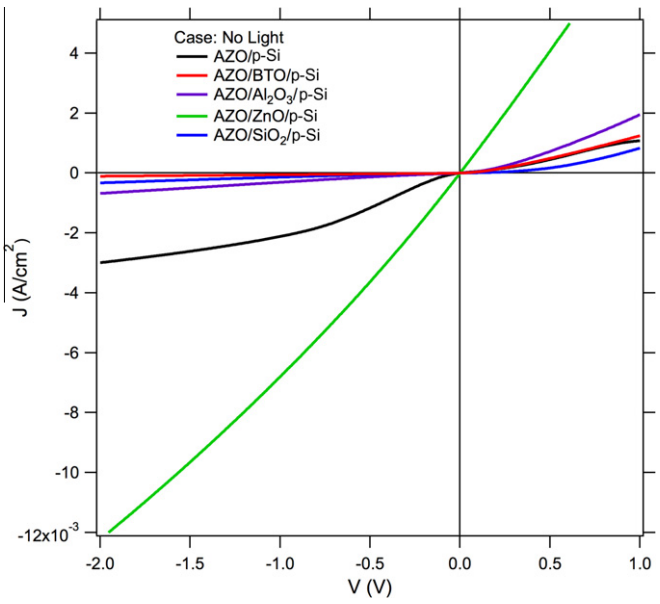

Figure 6. Dark current density vs. voltage characteristics of the AZO seed layer and various intermediate layers deposited on *p*-Si.

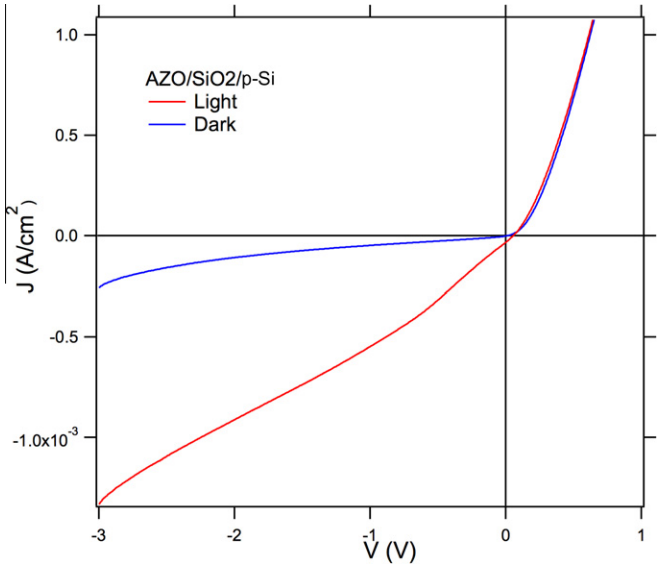

Figure 7. Current density vs. voltage characteristics of AZO/SiO_2/*p*-Si.

It widely known that the photovoltaic effect is due to the light activated electron generation at the depletion region of the *p*-Si, notably near the heterojunction interface. Al:ZnO film is highly transparent ($T > 90\%$) in the visible region, and that allows the visible light to pass through AZO film. For AZO/*p*-Si heterojunction, the light is primarily absorbed in the underlying *p*-Si layer. This generates electron–hole pairs, producing the photocurrent under reverse bias conditions [19]. As the UV photons are primarily absorbed in the AZO layer the photo-generated electrons diffuse towards the positive electrode through the AZO region. This gives rise to the increase in current almost linearly as the reverse bias increases as shown in all samples. On the other hand, the *P*-type silicon surface provides a supply of elections, which can enter into the AZO film. The effective coupling current flows due to the interchange of the charge between the conduction and valence-bands of the silicon by recombination and generation [19]. However, due to linear increase in current with increasing reverse bias, the diode characteristic did not arise. In order to see this effect, various intermediate layers where deposited between the AZO and *p*-Si layers. It was found that the AZO/SiO_2/*p*-Si heterojunction with SiO_2 as an insulating barrier displayed a good rectifying diode behavior [20,21]. Due to its rectifying behavior, we proceeded to investigate the following device structure with an AZO nanorod arrays grown on the AZO seed layer.

Figure 8 shows the current density vs. voltage characteristics of AZO/SiO_2/*p*-Si (SL) and AZONRs/AZO/SiO_2/*p*-Si (NR). The AZO nanorod array grown on the AZO film comprised of 5% Al doping using 0.05 M $AlCl_3$. The dark leakage current density is about 0.8 mA/cm^2 in the reverse bias region. As stated earlier, the dark leakage current density is about 0.8 mA/cm^2 in the reverse bias region. The dark leakage current was reduced, while its photocurrent induced under illumination was noticeably larger. It is known that under reverse bias, the current is affected by light. Under light, the

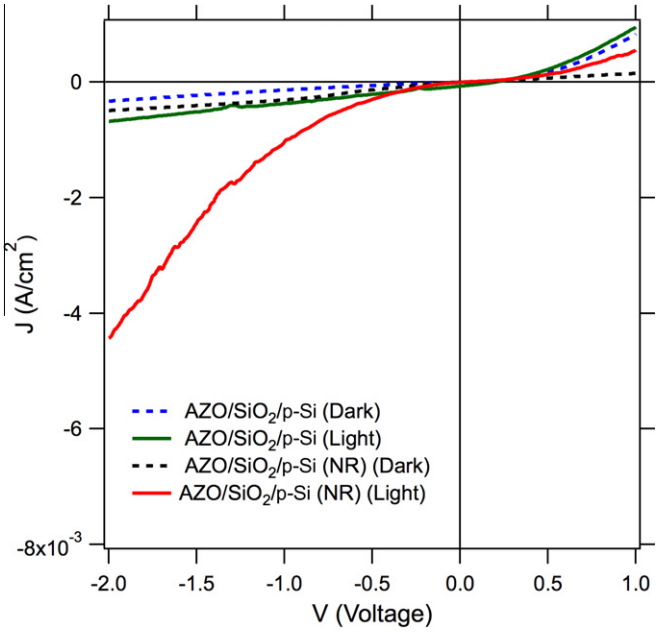

Figure 8. Current density vs. voltage characteristics of AZO/SiO_2/*p*-Si with and without nanorod arrays.

photogenerated current density is about 5 mA/cm^2 in the reverse bias region. As stated earlier, the photogenerated current density is about 0.7 mA/cm^2 in the reverse bias region. In the presence of light a photovoltaic behavior is observed. The inset in Figure 8 shows the photovoltaic effect of the photo current being generated for both samples showing a larger photovoltaic effect between the two. The short circuit current J_{sc} was about 2.38×10^{-6} A/cm^2, while the open circuit voltage V_{oc} is about 1.92×10^{-2} V. In order to see this effect, the AZO/SiO_2/*p*-Si heterojunction was illuminated under the halogen lamp with 1 W/cm^2 in order to observe the photovoltaic effect. The nanorods were grown on AZO/SiO_2/*p*-Si heterojunction. The photocurrent is significantly reduced in nanorod arrays on AZO/SiO_2/*p*-Si heterojunction due to multiple scattering phenomena associated with the nanorod arrays, which are very much single crystalline. The hexagonal facets of ZnO nanorods initiate the multiple scattering and will be discussed elsewhere in detail. However, this research may open up venues for various optical and opto-electronic applications where highly aligned nanostructures are desired. Further work in progress in order to study the effects of alignment of nanorod arrays on the photovoltaic properties.

4. Conclusion

We have demonstrated the growth of almost perfectly vertically aligned ZnO nanorod arrays synthesized by the hydrothermal route on a sputtered Al:ZnO seed layer on Si using different growth strategies. The well-aligned nanorods were grown at considerably lower temperature on a seed layer, however but without any template. The nanorod arrays demonstrate remarkable alignment along the *c*-axis over a large area. Several barrier layers, such as Al_2O_3, $BaTiO_3$ and SiO_2 were introduced to form the p-i-n junction to reduce the leakage current between Al:ZnO and *p*-Si. The photocurrent is significantly reduced in nanorod arrays on AZO/SiO_2/*p*-Si heterojunction due to multiple scattering phenomena associated with the nanorod arrays. This research may open up venues for various optical and opto-electronic applications where highly aligned nanostructures are desired.

Acknowledgements

This work is supported by the DoD (CEAND) Grant No. W911NF-11-1-0209 (US Army Research Office), NSF-CREST (CNBMD) Grant No. HRD 1036494 and NSF-RISE Grant No. HRD-0931373. The authors are thankful to R.B. Konda for experimental help.

Appendix A. Supplementary data

Supplementary data associated with this article can be found, in the online version, at http://dx.doi.org/10.1016/j.cplett.2012.03.028.

References

[1] C.J. Lee, T.J. Lee, S.C. Lyu, Y. Zhang, H. Ruh, H.J. Lee, Appl. Phys. Lett. 81 (2002) 3648.
[2] W.I. Park, G.C. Yi, Adv. Mater. 16 (2004) 87.
[3] L. Vayssieres, K. Keis, A. Hagfeldt, S.-E. Lindquist, J. Phys. Chem. B 105 (2001) 3350.
[4] L. Vayssieres, Adv. Mater. 15 (2003) 464.
[5] D.C. Olson, J. Piris, R.T. Collins, S.E. Shaheen, D.S. Ginley, Thin Solid Films 496 (2006) 26.
[6] K. Takanezawa, K. Hirota, Q.S. Wei, K. Tajima, K. Hashimoto, J. Phys. Chem. C 111 (2007) 7218.
[7] B. O'Regan, M. Grätzel, Nature 353 (1991) 737.
[8] Y.Y. Lin et al., J. Mater. Chem. 17 (2007) 4571.
[9] G.-C. Yi, C. Wang, W.I. Park, Semicond. Sci. Technol. 20 (2005) S22.
[10] C. Fournier, O. Bamiduro, H. Mustafa, R. Mundle, R.B. Konda, F. Williams, A.K. Pradhan, Semicond. Sci. Technol. 23 (2008) 085019.
[11] E.A. Davis, N.F. Mott, Phil. Mag. 22 (1970) 903.
[12] V. Bhosle, A. Tiwari, J. Narayan, Appl. Phys. Lett. 88 (2006) 032106.
[13] O. Bamiduro, H. Mustafa, R. Mundle, R.B. Konda, A.K. Pradhan, App. Phys. Lett. 90 (2007) 252108.
[14] Y. Furubayashi et al., Appl. Phys. Lett. 86 (2005) 252101.
[15] R.C. Budhani, P. Pant, R.K. Rakshit, K. Senapati, S. Mandal, N.K. Pandey, J. Kumar, J. Phys.: Condens. Matter 17 (2005) 75.
[16] K. Lord, T.M. Williams, D. Hunter, K. Zhang, J. Dadson, A.K. Pradhan, Appl. Phys. Lett. 88 (2006) 262105.
[17] A.K. Pradhan, L. Douglas, H. Mustafa, R. Mundle, D. Hunter, C.E. Bonner, Appl. Phys. Lett. 90 (2007) 072108.
[18] Maria Letizia Terranova, S. Orlanducci, Antonio Serra, Daniela Manno, Emanuela Filippo, Marco Rossi, Chem. Phys. Lett. 509 (2011) 152.
[19] H. Bo et al., Opt. Appl. 40 (2010) 15.
[20] Terence Holloway, Rajeh Mundle, Hareesh Dondapati, M. Bahoura, A.K. Pradhan, J. Nanophotonics (submitted).
[21] A.K. Pradhan, Terence Holloway, Rajeh Mundle, Hareesh Dondapati, M. Bahoura, Appl. Phys. Lett. 100 (2012) 061127.